



Synthesis and up-conversion luminescence properties of rare earth (Ce, Dy, Yb, and Er) doped CaF₂ nanoparticles

Ran Tian^a, Zhi-Jiang Yin^{a,*}, Hui Li^{a,*}, Ji Yang^a, Wen-Yuan Wang^a, Yu-Qiang An^a, Li-Jun Wu^a, Ze-Yuan Yang^b, Xing Yang^b, Zhen-Hua Ge^{b,*}

^a R&D Center of China Tobacco Yunnan Industrial Co., Ltd, Kunming 650032, China

^b Faculty of Materials Science and Engineering, Kunming University of Science and Technology, Kunming 650093, China



ARTICLE INFO

Keywords:
CaF₂ nanoparticles
Hydrothermal method
Rare earth doping
Upconversion luminescence performance

ABSTRACT

Calcium fluoride (CaF₂) possesses a wide bandgap, enabling it to exhibit upconversion luminescence (UCL) across a broad range of absorption spectra. The UCL performance is influenced by factors such as particle size, dispersion homogeneity, and the synthesis method. In this study, CaF₂ nanoparticles with a uniform microstructure were successfully synthesized using a hydrothermal technique by adjusting the reaction duration and temperature. The effect of rare-earth doping on the upconversion properties of the CaF₂ samples was evaluated, with Er doping used to examine the UCL performance. The findings indicate that the incorporation of the Er element into the CaF₂ lattice reduces the bandgap, which facilitates energy transfer, thereby enhancing the UCL performance of the Er-doped samples. The Ca_{0.97}Er_{0.03}F₂ sample exhibits the highest upconversion intensity at a power density of 52.28 W/cm², highlighting its significant potential for applications in laser technology, display systems, optical storage, information security, biological imaging, and medical diagnosis and treatment.

1. Introduction

Upconversion luminescence (UCL) has garnered considerable and consistent scholarly interest since its discovery in the 1960s [1]. And with the development of UCL technology, which has evolved into a prominent area of focus within materials science and condensed matter physics research [2–4]. UCL involves the production of high-frequency photon emission through a two-photon or multi-photon process [5] initiated by low-frequency photon absorption and proceeds through intermediate energy states [6]. In comparison to traditional two-photon or multi-photon absorption processes, the upconversion light-emitting pumping mechanism eliminates the need for phase matching and offers higher excitation efficiency [7,8]. This allows for the utilization of a low-power density near-infrared laser diode as the pumping light source. Due to its distinctive nonlinear emission process, UCL finds diverse applications in solid-state lasers, infrared detection, anti-counterfeiting, sensing, photocatalysis, energy spectrum conversion for solar cells, and biological fields [9–12].

In recent years, the doping of rare-earth ions into host matrices has been extensively used to investigate transparent and luminescence properties, with particular emphasis on Er. Numerous studies have

shown that the addition of various impurity ions, such as Gd³⁺, Mg²⁺, and Li⁺, alongside Er³⁺/Yb³⁺ or Ho³⁺/Yb³⁺ doping [13–17], can markedly enhance the UCL performance of phosphors. These impurity ions effectively modify the crystal structure and significantly enhance the UCL intensity [18]. Notably, the luminescent behavior of upconversion materials is strongly influenced by the choice of host materials [19,20]. The rare earth Eu and Er are introduced to tuning the UCL properties, which possess multiple luminescent centers and a stable phase structure, and facilitates the realization of thermoresponsive luminescence [21]. Furthermore, lanthanide ions, especially Er³⁺ and Yb³⁺, exhibit similar spectral overlaps, which is conducive to promoting the production of UCL [14]. Feenstra et al. [13] showed that Er³⁺/Yb³⁺ upconverters broaden the effective absorption band of solar cells and enhance UCL when embedded in an aluminosilicate glass matrix. Hua et al. examined the underlying upconversion mechanism in these systems [22], emphasizing that fluoride hosts—owing to their low phonon energies—minimize nonradiative losses and thereby enhance upconversion efficiency. In addition, the close ionic radii of trivalent rare-earth ions permit facile substitution for Ca²⁺ sites, while interstitial F⁻ ions enable charge compensation.

Thus, CaF₂ is widely employed as a host matrix for UCL studies as it

* Corresponding authors.

E-mail addresses: yinj@ynzy-tobacco.com (Z.-J. Yin), lhui@ynzy-tobacco.com (H. Li), zge@kust.edu.cn (Z.-H. Ge).

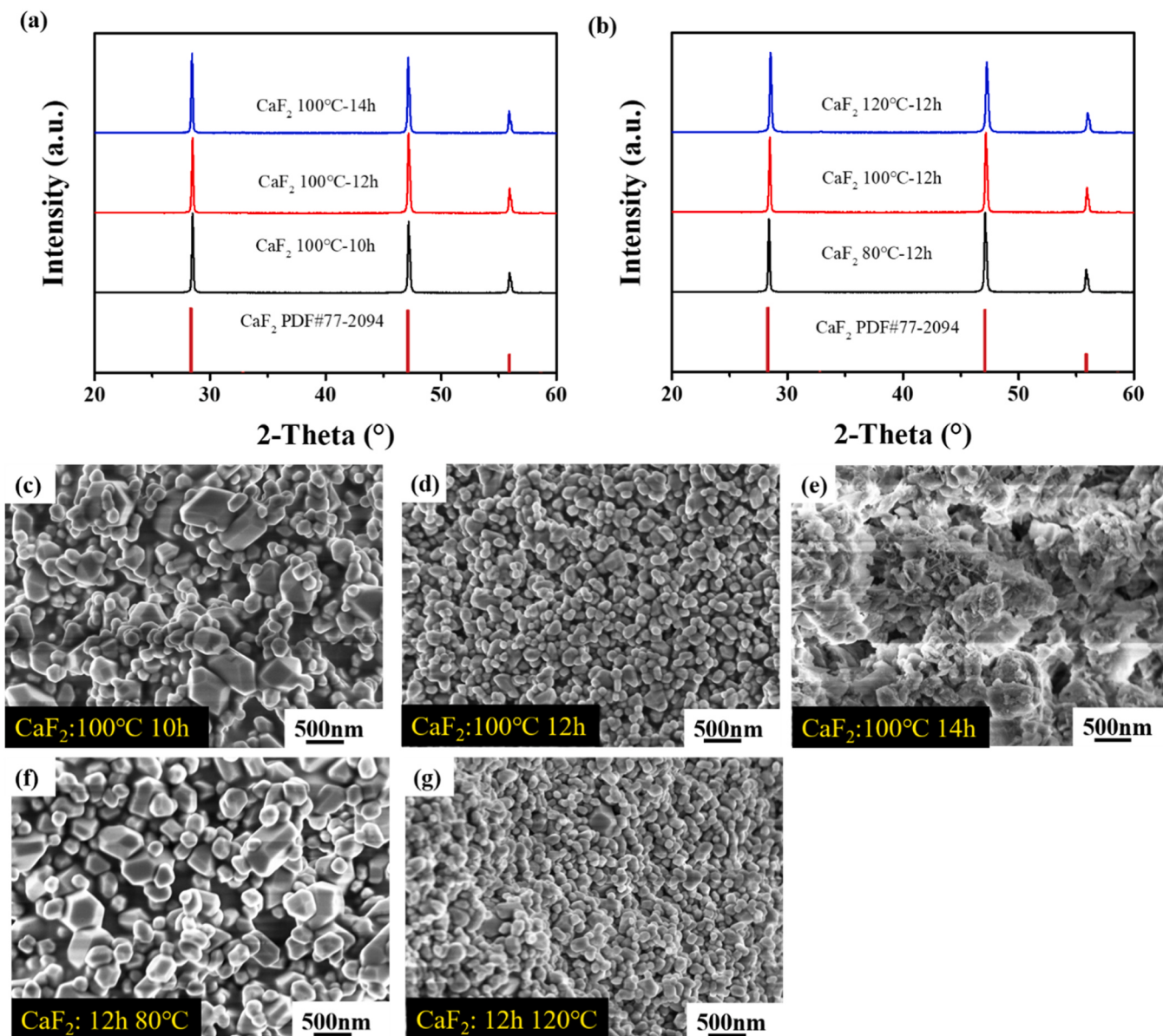


Fig. 1. XRD patterns of CaF₂ powders with (a) different reaction times, (e) different reaction temperatures. SEM images of CaF₂ powders with different reaction times in 100 °C: (b) 10 h, (c) 12 h, and (d) 14 h; with different reaction temperatures in 12 h: (f) 80 °C, (g) 100 °C, and (h) 120 °C.

possesses metastable electronic energy levels that can be stimulated by nonradiative transitions and subsequently emit photons [23–26]. However, undoped CaF₂ exhibits limited upconversion efficiency. To overcome this limitation and broaden its applicability, rare-earth ions have been introduced into the CaF₂ matrix [27–29]. For instance, Liu et al. [30] demonstrated that CaF₂ ceramics exhibited high optical transmittance, reaching 44.9 % at 500 nm and 53.6 % at 1200 nm upon the introduction of Er ions. Yang et al. [31] prepared CaF₂ nanopowders doped with Ln³⁺ (Ln = Er, Nd, and Yb) using a hydrothermal method and investigated the use of chelating agents to form hierarchical nano-flowers. In addition, the samples demonstrated favorable properties across the spectral region from 1300 to 1600 nm, suggesting their potential for applications in the telecommunication field.

Herein, CaF₂ nanopowders with a uniform microstructure were synthesized by tuning the reaction time and temperature during the hydrothermal method. However, the pure CaF₂ sample exhibited very poor UCL. To enhance this performance, various rare earth elements (Ce³⁺, Dy³⁺, Yb³⁺, and Er³⁺) were screened, and Er doping in the CaF₂ lattice proved remarkably effective. The effect of Er content on the

upconversion properties of the CaF₂ matrix was systematically investigated. The results showed that Er doping narrowed the bandgap and markedly increased UCL intensity. Among the compositions studied, Ca_{0.97}Er_{0.03}F₂ exhibited the highest spectral intensity under 980 nm laser excitation at a power density of 52.28 W/cm². These findings highlight that Er-doped CaF₂ is a promising candidate for applications in biological imaging, diagnosis and treatment, panchromatic displays, and information security.

2. Experimental section

In this experiment, CaF₂ samples were synthesized via a hydrothermal method using CaCl₂·2H₂O, NH₄F, Ce(NO₃)₃·6H₂O, Dy(NO₃)₃·5H₂O, Yb(NO₃)₃·5H₂O, and Er(NO₃)₃·5H₂O. The synthesis was performed by mixing CaCl₂·2H₂O (1.47 g) and NH₄F (0.74 g) in 50 mL of deionized water, followed by stirring for approximately 10 min to obtain a transparent solution serving as the CaF₂ source. Separately, x mmol of Re (NO₃)₃·bH₂O (Ce(NO₃)₃·6H₂O, Dy(NO₃)₃·5H₂O, Yb(NO₃)₃·5H₂O, and Er(NO₃)₃·5H₂O) powders were dissolved in deionized water after

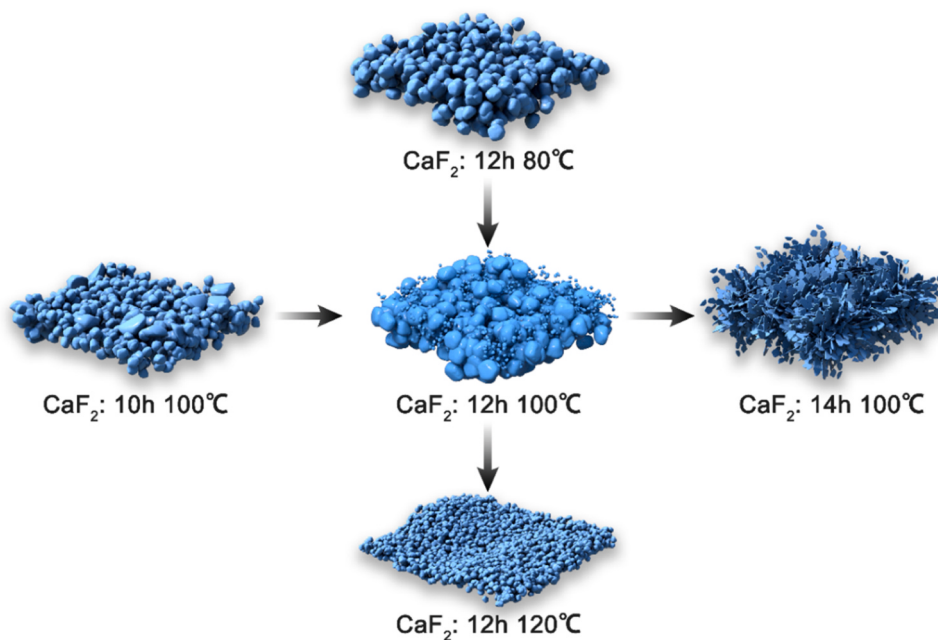


Fig. 2. Sketch map of the variation in the morphology and size of CaF_2 crystals under different conditions.

stirring for about 10 min. The entire solution was then transferred into a 100 mL Teflon-lined stainless-steel autoclave. For the hydrothermal synthesis of nano-sized CaF_2 , lower temperatures and shorter reaction times were initially employed, and these parameters were gradually optimized. Various temperatures (80°C , 100°C , 120°C) and reaction times (10 h, 12 h, 14 h) were selected. The resulting $\text{Ca}_{1-x}\text{A}_x\text{F}_2$ ($\text{A} = \text{Ce}, \text{Dy}, \text{Yb}, \text{and Er}; x = 0, 0.01, 0.03, \text{ and } 0.05$) products were collected by centrifugation, washed several times with deionized water and ethanol, and dried under vacuum at 60°C for 8 h.

The experiment utilized the MiniFlex600 X-ray diffractometer manufactured by Rigaku Corporation, Japan. The main experimental parameters were as follows: Cu target with $\text{K}\alpha$ radiation, tube voltage of 30 kV, tube current of 20 mA, continuous scanning with a step size of 0.02° , scanning rate of $10^\circ/\text{min}$, and a scanning range of $20^\circ\text{--}80^\circ$. All measurements were conducted at room temperature. Scanning electron microscopy (SEM) is a commonly used characterization tool for observing the surface morphology and microstructure of materials. Ultraviolet-visible (UV-Vis) spectroscopy (Shimadzu UV-3600-plus, Shimadzu Corporation, Japan) is used to measure the absorption and transmission of light by samples in the ultraviolet and visible regions. Furthermore, a 980 nm laser served as the excitation source for measuring the UCL of the sample at a power density of 52.28 W/cm^2 at room temperature (HITACHIU-F-7000, Japan). Transmission electron microscopy (HRTEM) images were acquired to study the microstructure of the materials, including crystal structures, lattice defects, grain boundaries, and nanostructures. Such analysis is crucial for understanding material properties and performance, contributing to the development of new materials.

First-principles calculations were performed using the Vienna *ab initio* simulation package (VASP) based on density functional theory (DFT) for both the pristine and Er-doped CaF_2 samples, employing the Perdew–Burke–Ernzerhof model. A plane-wave cutoff energy was set at 560 eV, and a Gaussian smearing width of 0.05 eV was applied to accurately describe the orbital occupancies. The Brillouin zone was sampled using the Monkhorst–Pack scheme with a $2 \times 2 \times 5$ k-point mesh, whose correctness was confirmed through a convergence test with higher k-point densities. Electronic energies and atomic forces were converged to thresholds of 10^{-6} eV and $-0.05 \text{ eV}/\text{\AA}$, respectively. All calculations utilized $2 \times 2 \times 1$ supercells consisting of 48 atoms. To determine the most stable structural arrangement of the Er-doped

system, all imaginable non-equivalent, singly disordered configurations were evaluated. Subsequently, the configuration with the lowest total energy was selected.

3. Results and discussion

3.1. Synthesis of pure CaF_2 with uniform microstructure

The synthesis of homogeneous CaF_2 powders was examined by adjusting the reaction time and temperature. At a constant temperature of 100°C , reaction times of 10 h, 12 h, and 14 h were explored, demonstrating that the energy of the reaction system exhibits an upward trend with longer reaction times. The phase structure of CaF_2 samples was analyzed through X-ray diffraction (XRD), as shown in Fig. 1a. The primary diffraction peaks of the CaF_2 samples synthesized at varying reaction times are aligned with the standard PDF card (PDF#77–2094), corresponding to the $Fm\text{-}3m$ (225) space group, with no secondary phases detected. Fig. 1c–e illustrates the morphology of CaF_2 powders subjected to varying reaction durations. At a reaction time of 10 h, the CaF_2 product consists of both small and large particles. The formation of larger particles may be attributed to grain aggregation, driven by the Ostwald ripening phenomenon. As the reaction time increases, the energy of the reaction system escalates, resulting in the growth of smaller grains into larger ones, akin to the typical CaF_2 grains. With further extension of the reaction time, several larger and more uniform particles are generated, leading to the development of an irregular lamellar structure due to the prolonged duration. Thus, a reaction time of 12 h was selected. Furthermore, the reaction temperature was monitored over a period of 12 h, as illustrated in Fig. 1b. The principal diffraction peaks of the CaF_2 samples at different reaction temperatures match the standard PDF card (PDF#77–2094), with no evidence of secondary phases. Fig. 1d, g–h depicts the shape of CaF_2 powders obtained at various reaction temperatures. When the reaction period is fixed at 12 h, an increase in reaction temperature initially leads to smaller grains; however, a further rise in temperature to 120°C resulted in grain growth due to the formation of additional nuclei produced by the higher energy within the reaction system.

Based on the synthesis process described above, changes in the morphology of the crystalline grains with time and temperature were intuitively observed. During the hydrothermal reaction, the ideal

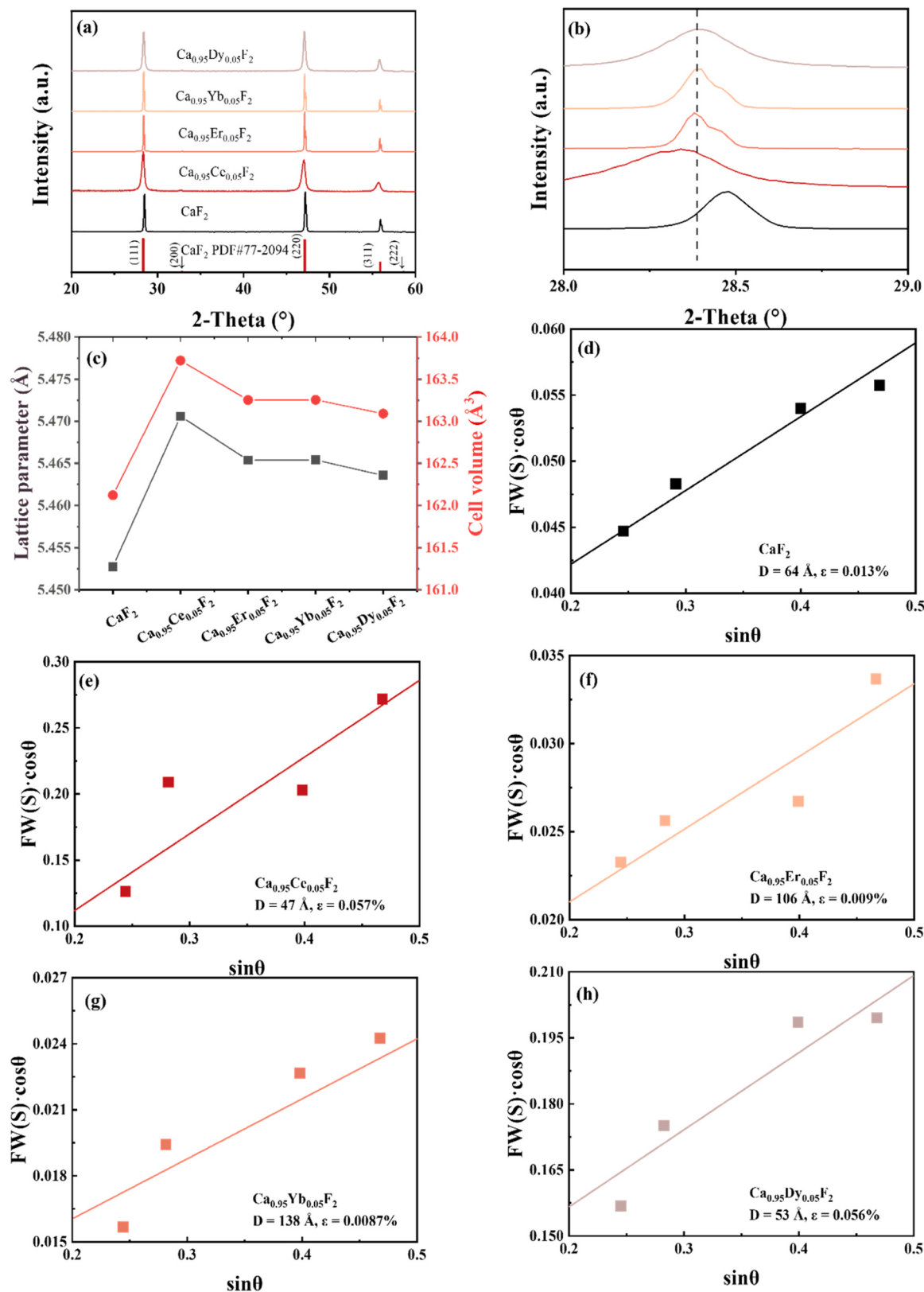


Fig. 3. (a) XRD patterns, (b) enlarged XRD patterns in 2-theta of 28° to 29° , (c) the lattice parameter and cell volume, and (d-h) W-H relationships of pristine and $\text{Ca}_{0.95}\text{A}_{0.05}\text{F}_2$ ($\text{A} = \text{Ce}, \text{Er}, \text{Yb}$, and Dy) samples.

Table 1
Ionic radius of Ca^{2+} , Ce^{3+} , Dy^{3+} , Yb^{3+} , and Er^{3+} .

Ionic	Ionic radius (\AA)
Ca^{2+}	1.06
Ce^{3+}	1.01
Dy^{3+}	0.912
Yb^{3+}	0.868
Er^{3+}	0.89

morphology, size distribution, and crystal structure of nano-sized CaF_2 particles were obtained by conducting the reaction at 120 °C for 12 h. The results indicate that the optimal conditions for the hydrothermal synthesis of CaF_2 are a reaction time of 12 h and a reaction temperature of 120 °C. The possible reaction mechanism is illustrated in Fig. 2.

3.2. Screening of rare earth elements

Using the above-mentioned synthesis process, rare earth elements were introduced into the CaF_2 matrix. Specifically, Ce, Dy, Yb, and Er were individually introduced to enhance the UCL performance. These dopants are usually employed to optimize and tune UCL properties [7, 24,28,32]. In the synthesis process of CaF_2 powders, each rare-earth ion

was doped separately, and the resulting samples were characterized by XRD. As shown in Fig. 3a, the diffraction peaks of all samples align well with the standard PDF card, indicating the successful incorporation of rare-earth ions into the CaF_2 lattice. To investigate the influence of different doped rare earth elements on the properties of CaF_2 , a fixed doping concentration of 5 mol% was maintained for each element, while the type of rare-earth ion (Ce^{3+} , Dy^{3+} , Yb^{3+} , and Er^{3+}) was varied. Fig. 3b depicts that diffraction peak offsets occur with varying degrees of angular displacement, and the XRD patterns of all doped samples shift toward lower angles. This shift suggests that rare-earth ions enter interstitial sites, leading to lattice expansion. Fig. 3c shows the lattice parameter and cell volume based on the refined XRD data for all samples. It is clearly seen that the lattice parameter increases when the rare earth elements are singly introduced in the CaF_2 lattice, demonstrating the lattice expansion on the side. The detailed ionic radii of rare-earth ions are provided in Table 1. It is observed that the FWHM of Ce and Dy doped sample is broader than other samples, the possible reasons may be the higher lattice strain caused by their larger ionic radius and the smaller grain size affected by the nucleation energy and growth rate of crystals. By further analyzing the XRD refinement data, the rare earth ions enter the CaF_2 lattice, the lattice strain of CaF_2 lattice changes, the relationships between lattice strain (ϵ), grain size (D), and full width at half maximum (FWHM) are shown in Fig. 3d-h. A higher lattice strain

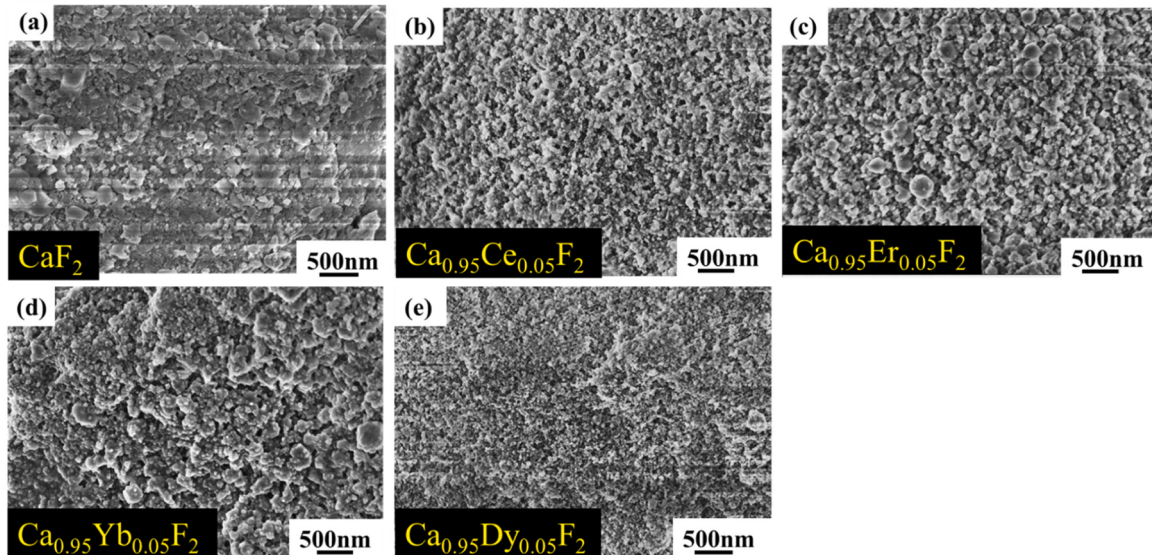


Fig. 4. SEM images of (a) undoped sample, (b) $\text{Ca}_{0.95}\text{Ce}_{0.05}\text{F}_2$, (c) $\text{Ca}_{0.95}\text{Er}_{0.05}\text{F}_2$, (d) $\text{Ca}_{0.95}\text{Yb}_{0.05}\text{F}_2$, and (e) $\text{Ca}_{0.95}\text{Dy}_{0.05}\text{F}_2$.

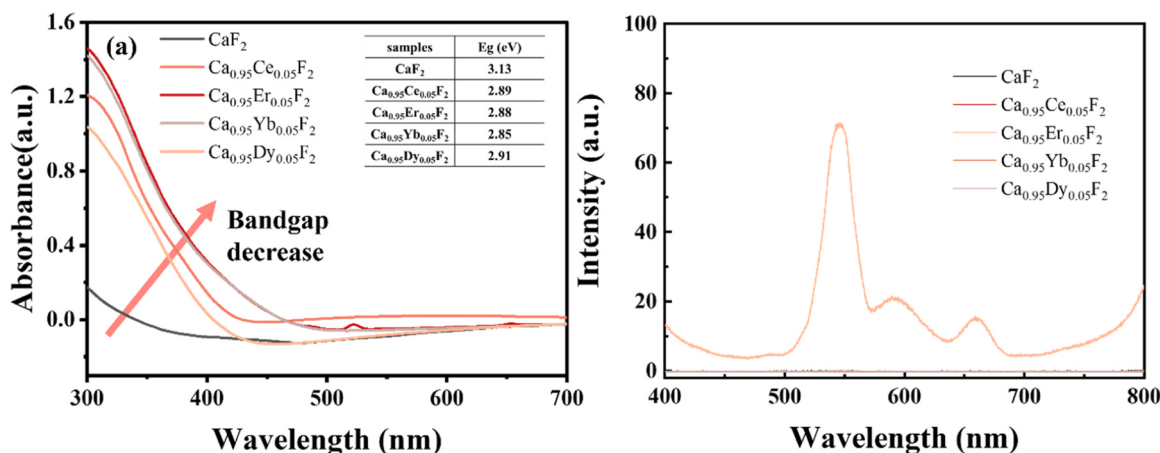


Fig. 5. (a) Absorbance and inserted bandgap values, and (b) Up-conversion luminescence spectra of $\text{Ca}_{0.95}\text{A}_{0.05}\text{F}_2$ ($\text{A} = \text{Ce}, \text{Er}, \text{Yb}$, and Dy) samples.

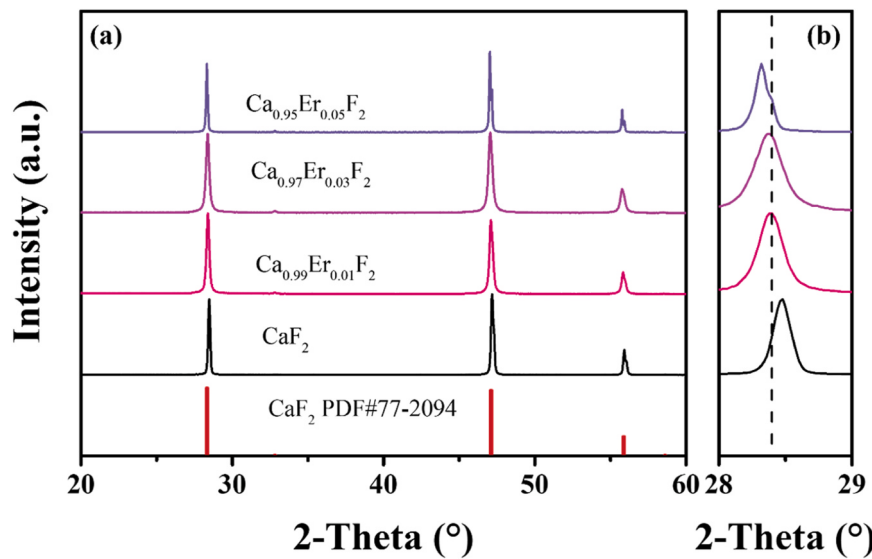


Fig. 6. (a) XRD patterns of $\text{Ca}_{1-x}\text{Er}_x\text{F}_2$ ($x = 0, 0.01, 0.03$, and 0.05) powders, (b) enlarged XRD patterns in 2-theta of 28° to 29° .

results in larger full width at half maximum, which in turn produces smaller grains. As shown in Fig. 3d-h and Table 1, the ionic radius increases sequentially from Er^{3+} , Yb^{3+} , Dy^{3+} to Ce^{3+} , when the rare earth ionic enters the CaF_2 lattice, the lattice strain increases as the ionic radius of rare earth increases. The lattice strain reaches to 0.057 % for the $\text{Ca}_{0.95}\text{Ce}_{0.05}\text{F}_2$ sample, which obtains the smallest grains (47 Å), and the $\text{Ca}_{0.95}\text{Yb}_{0.05}\text{F}_2$ sample achieves the smallest lattice strain value of 0.0087 % and the biggest grains of 138 Å.

The microstructure of $\text{Ca}_{0.95}\text{A}_{0.05}\text{F}_2$ ($\text{A} = \text{Ce}, \text{Dy}, \text{Yb}$, and Er) samples, presented in Fig. 4, shows that rare-earth doping affects grain growth. The agglomeration of nanopowders results in the formation of smaller grains in the pristine sample. However, with the introduction of rare-earth ions, the grain size of all doped samples increases due to atom diffusion, ultimately leading to the formation of larger particles. SEM images reveal an apparent increase in particle size following rare-earth

ion doping. The particle size distribution is shown in Fig. S1, indicating a noticeable aggregation of the grains.

As depicted in Fig. 5a, the bandgap (E_g) of all samples shows that E_g is narrowed owing to rare-earth doping in the CaF_2 matrix, consistent with observations reported in previous studies [33]. The introduction of rare earth elements into the CaF_2 samples resulted in a significant decrease in the energy bandgap, which is likely because of the formation of impurity levels in the doped samples, calculated by the relationship between E_g and λ_g ($E_g = 1240/\lambda_g$) [34]. Qualitative analysis further reveals a noticeable reduction in the bandgap after the doping process, with Er-doped CaF_2 exhibiting the lowest bandgap. This indicates that rare-earth doping has a pronounced effect on bandgap reduction. Notably, a lower energy band is more conducive to carrier transport. As shown in Fig. 5b, the doping of Ce, Dy, and Yb does not significantly improve the UCL performance of CaF_2 under a power density of

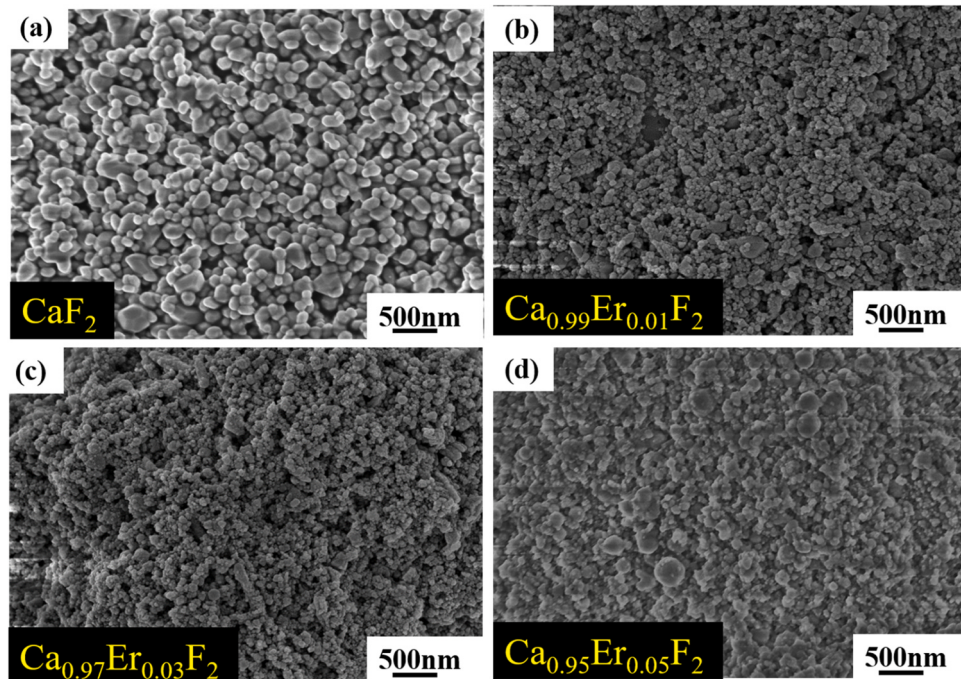


Fig. 7. SEM images of $\text{Ca}_{1-x}\text{Er}_x\text{F}_2$ ($x = 0, 0.01, 0.03$, and 0.05) powders.

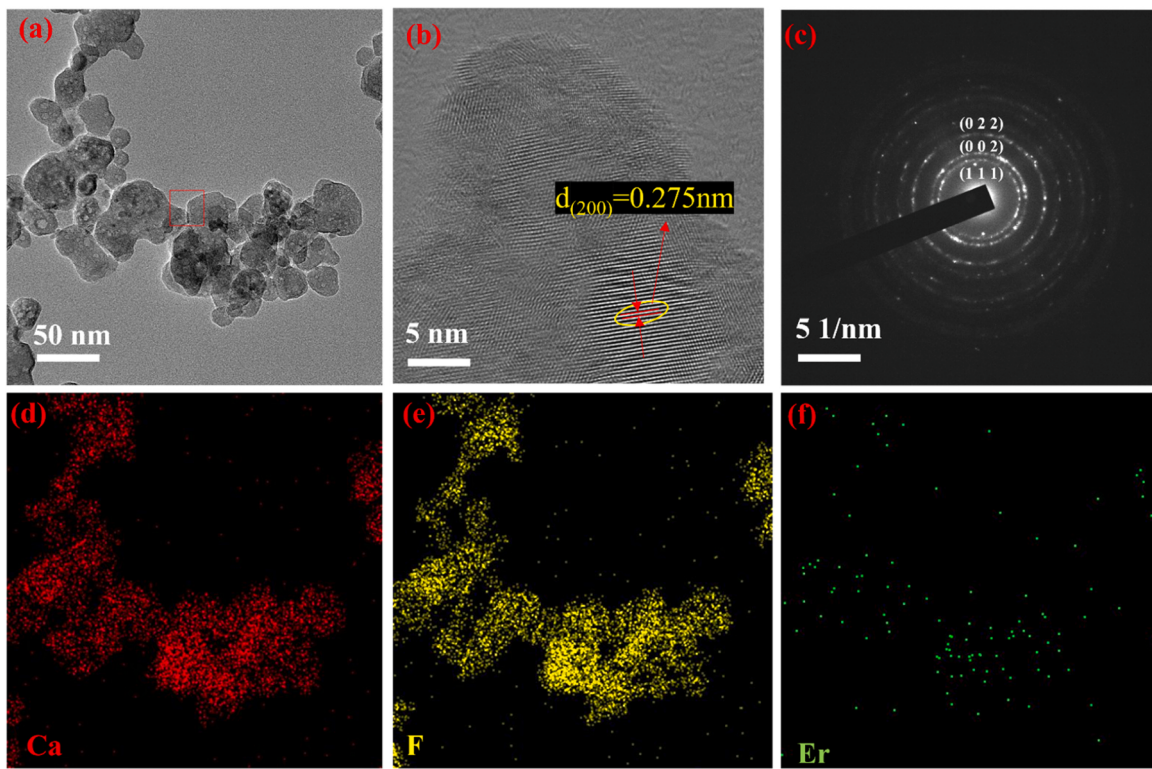


Fig. 8. TEM information of $\text{Ca}_{0.97}\text{Er}_{0.03}\text{F}_2$ sample (a) a typical TEM image, (b) HRTEM image, (c) FFT image, and EDS-mapping of the elements for (d) Ca, (e) F, and (f) Er.

52.28 W/cm² at room temperature. A notable intensity is found only when CaF_2 is doped with 5 mol% Er. Therefore, the investigation of Ce^{3+} , Dy^{3+} , and Yb^{3+} doping was discontinued, and subsequent experiments mainly focused on Er doping to explore the optimal concentration.

3.3. UCL enhanced by Er doping

To examine the phase structure, the XRD analysis was performed on the $\text{Ca}_{1-x}\text{Er}_x\text{F}_2$ ($x = 0, 0.01, 0.03$, and 0.05) samples. As displayed in Fig. 6, the prominent diffraction peaks of the CaF_2 samples correspond to the standard PDF card (PDF#77-2094), with no indication of secondary phases. As shown in Fig. 6b, a monotonic change is observed with increasing Er content, suggesting the successful incorporation of Er into the CaF_2 lattice. The XRD patterns shift to the lower angles, which can be attributed to Er^{3+} ions occupying interstitial sites, resulting in

lattice expansion. Meanwhile, when the Er content is less than 3 %, the XRD patterns shift to the lower angles, which can be attributed to Er^{3+} ions occupying interstitial sites, resulting in lattice expansion. However, when the Er content exceeds to 5 %, the diffraction peaks widen, and a smaller resolvable $\text{K}\alpha_2$ peak appears. Moreover, the grain size increases as Er^{3+} ions enter the CaF_2 matrix due to atomic diffusion, with particle size increasing as the Er^{3+} content increases (Fig. 7).

To further explore the microstructure of $\text{Ca}_{0.97}\text{Er}_{0.03}\text{F}_2$, high-resolution TEM (HRTEM) analysis was conducted, as shown in Fig. 8. The diffraction spots of the $\text{Ca}_{0.97}\text{Er}_{0.03}\text{F}_2$ sample belong to the standard XRD cards. Compared to the undoped sample ($d_{(200)} = 0.259 \text{ nm}$), the lattice of CaF_2 expands to 0.275 nm , indicating that the Er ions successfully enter the CaF_2 lattice, causing lattice expansion. The diffraction pattern reveals that the sample is polycrystalline in nature. Fig. 8d-f depicts the energy-dispersive X-ray spectroscopy (EDS) mapping results for the $\text{Ca}_{0.97}\text{Er}_{0.03}\text{F}_2$ sample, showing that the Ca, Er, and F elements are

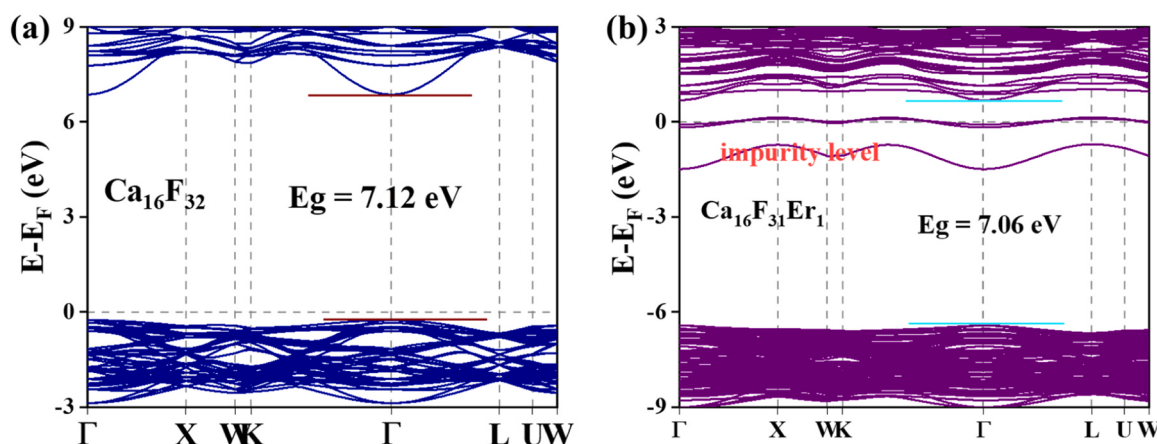


Fig. 9. The band gap of the (a) pristine sample and (b) Er-doped sample.

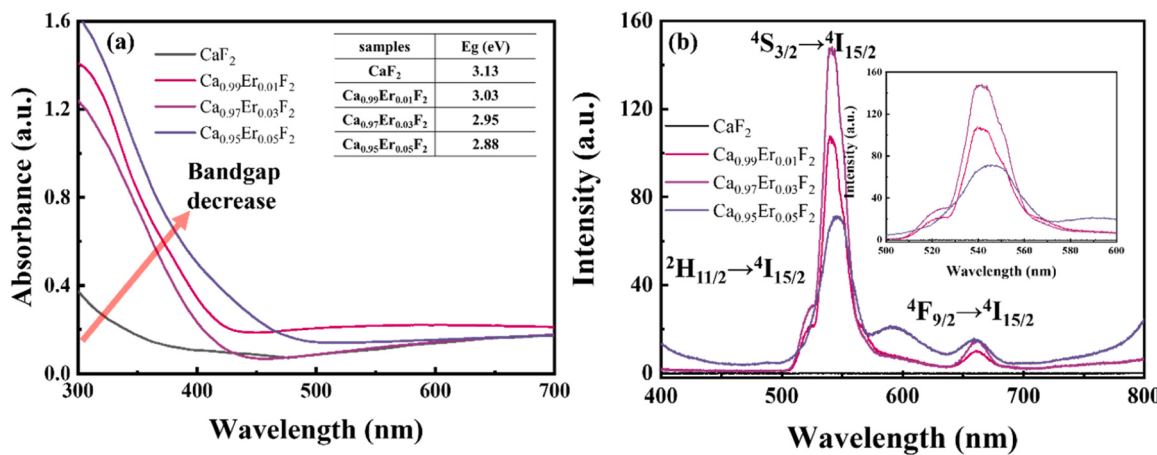


Fig. 10. (a) Absorbance and inserted bandgap values, and (b) Up-conversion luminescence spectra of Ca_{1-x}Er_xF₂ (x = 0, 0.01, 0.03, and 0.05) samples.

evenly distributed throughout the sample. These results further validate the successful formation of the proposed Ca_{0.97}Er_{0.03}F₂ material.

The results of the DFT calculations for both the pristine and Er-doped CaF₂ samples are shown in Fig. 9. Upon the introduction of Er into the CaF₂ matrix, the band gap decreases, which facilitates the release of electron carriers. Additionally, an impurity level is generated within the energy band of the Er-doped sample, promoting electron transport.

Furthermore, the UCL properties of Ca_{1-x}Er_xF₂ (x = 0, 0.01, 0.03, and 0.05) samples were investigated. As shown in Fig. 10a, Er doping in the CaF₂ matrix initially reduces the bandgap; however, a further increase in Er content induces a widening of the bandgap. This behavior may reflect phase-structural changes, as reported elsewhere [35], and is corroborated by our DFT results. Fig. 10b displays the fluorescence spectra obtained under 980 nm laser excitation. The UCL intensity initially increases with Er concentration up to 3 mol%, then declines at higher concentrations. The highest luminescence intensity is achieved at 3 mol % Er. The broad spectral profile is ascribed to the absence of a photosensitizer, leading to the observation of additional peaks. Besides, the base peaks noted are inherent to the measurement process and are inevitable. The primary peaks appear at approximately 525 nm, 560 nm, and 670 nm. The upconversion mechanism of Er³⁺ doping in the CaF₂ matrix is as follows: two main luminescence bands are present in the range of 520–560 nm (green luminescence) and 640–670 nm (red luminescence). These bands are assigned to the ²H_{11/2}, ⁴S_{3/2} → ⁴I_{15/2} and ⁴F_{9/2} → ⁴I_{15/2} transitions, respectively. As the Er content increases, intense red emissions with relatively weakened green emissions are observed. This effect may result from cross-relaxation processes in Er³⁺ ions at higher concentrations, which play a significant role in depopulating the ²H_{11/2} and ⁴S_{3/2} levels. Therefore, the Ca_{0.97}Er_{0.03}F₂ sample exhibits superior UCL performance.

4. Conclusions

CaF₂ nanopowders were synthesized by tuning the reaction time and temperature using a hydrothermal method, with the optimal reaction conditions determined to be 12 h at 120 °C. However, the UCL of the pristine CaF₂ sample was found to be poor under 980 nm excitation. To enhance this performance, Er³⁺ ions were introduced, which altered the energy band of the doped samples. Further investigation into varying the Er content demonstrated that a higher concentration of Er doping in the CaF₂ matrix enhanced the green luminescence. The results revealed the highest upconversion performance in the Ca_{0.97}Er_{0.03}F₂ sample under a power density of 52.28 W/cm² at room temperature with 980 nm laser excitation. This material shows potential applications in biological imaging, diagnosis and treatment, panchromatic displays, and information security.

CRediT authorship contribution statement

Hui Li: Writing – review & editing, Investigation. **Zhi-Jiang Yin:** Writing – review & editing, Visualization, Methodology, Investigation. **Ran Tian:** Writing – original draft, Investigation, Funding acquisition. **Ge Zhenhua:** Writing – review & editing, Methodology. **Xing Yang:** Investigation. **Ze-Yuan Yang:** Investigation. **Li-Jun Wu:** Investigation. **Yu-Qiang An:** Investigation. **Wen-Yuan Wang:** Investigation. **Ji Yang:** Methodology, Investigation.

Declaration of Competing Interest

The authors declare no conflict of interest.

Acknowledgement

This work was supported by the Science and Technology Project of China Tobacco Yunan Industrial Co., Ltd. (Grant No. 2023CP05) and Outstanding Youth Fund of Yunnan Province (Grant No. 202201AV070005).

Appendix A. Supporting information

Supplementary data associated with this article can be found in the online version at doi:10.1016/j.mtcomm.2025.113248.

Data Availability

Data will be made available on request.

References

- [1] P.P. Sorokin, M.J. Stevenson, Stimulated infrared emission from trivalent uranium, Phys. Rev. Lett. 5 (1960) 557–559.
- [2] R.H. Banerjee, R. Alexander, N. Chaudhary, A.P. Srivastava, A.K. Debnath, V. Sudarsan, P. Sengupta, Structural characterization, defect evolution and luminescence properties of natural CaF₂ under 10 MeV electron irradiation, Ceram. Int. 49 (2023) 21324–21334.
- [3] T. Paik, N.J. Greybush, S. Najmr, H.Y. Woo, S.V. Hong, S.H. Kim, J.D. Lee, C. R. Kagan, C.B. Murray, Shape-controlled synthesis and self-assembly of highly uniform upconverting calcium fluoride nanocrystals, Inorg. Chem. Front. 11 (2024) 278–285.
- [4] B. Yuan, M. Li, C. Zhang, Calcination-assisted hydrothermal crystallization and comparative up-/down-conversion luminescence of RE³⁺ (RE=Ho, Er and Tm)-doped YbNbO₄ and Yb₃NbO₇, Mater. Today Commun. 41 (2024) 110860.
- [5] E. Cantelar, G. Lifante-Pedrola, M. Quintanilla, J.A. Sanz-García, F. Cussó, Spectroscopic characterization of Er³⁺-doped CaF₂ nanoparticles: luminescence concentration quenching, radiation trapping and transition probabilities, J. Alloy. Compd. 954 (2023) 170192.

- [6] J. Chen, W. Zhang, S. Cui, X. Peng, F. Hu, R. Wei, H. Guo, D. Huang, Up-conversion luminescence properties and temperature sensing performances of Ba₅Y₈Zn₄O₂₁: Yb³⁺, Er³⁺ phosphors, *J. Alloy. Compd.* 875 (2021) 159922.
- [7] Y. Cheng, Y. Wang, F. Teng, H. Dong, L. Chen, J. Mu, Q. Sun, J. Fan, X. Hu, H. Miao, Down-conversion emission of Ce³⁺-Tb³⁺ co-doped CaF₂ hollow spheres and application for solar cells, *Mater. Res. Express* 5 (2018) 036206.
- [8] M. Faustini, L. Nicole, E. Ruiz-Hitzky, C. Sanchez, History of organic-inorganic hybrid materials: prehistory, art, science, and advanced applications, *Adv. Funct. Mater.* 28 (2018) 1704158.
- [9] E.H.H. Hasabeldaim, H.C. Swart, R.E. Kroon, Luminescence and stability of Tb doped CaF₂ nanoparticles, *RSC Adv.* 13 (2023) 5353–5366.
- [10] Z. Guan, Y. Duan, X. Li, R. Shen, S. Xu, J. Sun, Y. Cao, Y. Wang, X. Zhang, B. Chen, Up-conversion luminescence properties and temperature sensing behavior of Nd³⁺/Yb³⁺/Tm³⁺ triply doped LaNbO₄ phosphors under 808 nm and 980 nm excitations, *Radiat. Phys. Chem.* 190 (2022) 109786.
- [11] M. Jin, K. Chang, C. Li, R. Zhang, Z. Li, X. Wang, K. Chen, PECVD-derived graphene saturable absorber mirror for 2.8 μm pulsed Er:ZBLAN fiber laser, *J. Phys. D Appl. Phys.* 55 (2022) 424007.
- [12] E. Liu, L. Lei, R. Ye, D. Deng, S. Xu, Improved relative temperature sensitivity of over 10% K⁻¹ in fluoride nanocrystals via engineering the interfacial layer, *Chem. Commun.* 58 (2022) 9076–9079.
- [13] J. Feenstra, I.F. Six, M.A.H. Asselbergs, R.H. van Leest, J. de Wild, A. Meijerink, R. E.I. Schropp, A.E. Rowan, J.J. Schermer, Er³⁺/Yb³⁺ upconverters for InGaP solar cells under concentrated broadband illumination, *Phys. Chem. Chem. Phys.* 17 (2015) 11234–11243.
- [14] R.E. Rojas-Hernandez, L.F. Santos, R.M. Almeida, Up-conversion enhancement in Er³⁺/Yb³⁺ doped 1-D microcavity based on alternating aluminosilicate glass and titania sol-gel layers, *Ceram. Int.* 46 (2020) 26273–26281.
- [15] B.C. Jamaliah, Tm³⁺ doped CaF₂ based oxyfluoroborosilicate glasses and glass ceramics for visible and NIR lasers, *J. Lumin.* 277 (2025) 120978.
- [16] N. Dubey, S. Gupta, S.B. Shelar, K.C. Barick, S. Chandra, Maximizing upconversion luminescence of co-doped CaF₂:Yb, Er nanoparticles at low laser power for efficient cellular imaging, *Molecules* 29 (2024) 4177.
- [17] Z. Zhang, J. Liu, Y. Wang, F. Ma, S. Liu, Z. Zhang, J. Liu, L. Su, Study on spectral properties and mid-infrared laser performance of Er, La:CaF₂ crystals, *Crystals* 14 (2024) 639.
- [18] Y. Yang, W. Li, B. Mei, J. Song, G. Yi, Z. Zhou, J. Liu, Synthesis and enhanced upconversion luminescence upon two-wavelength excitation of Er³⁺:CaF₂ transparent ceramics, *J. Lumin.* 213 (2019) 504–509.
- [19] M. Zahedifar, E. Sadeghi, S. Harooni, Thermoluminescence characteristics of the novel CaF₂:Dy nanoparticles prepared by using the hydrothermal method, *Nucl. Instrum. Meth. B* 291 (2012) 65–72.
- [20] C. Zhang, C. Li, C. Peng, R. Chai, S. Huang, D. Yang, Z. Cheng, J. Lin, Facile and controllable synthesis of monodisperse CaF₂ and CaF₂:Ce³⁺/Tb³⁺ hollow spheres as efficient luminescent materials and smart drug carriers, *Chem* 16 (2010) 5672–5680.
- [21] C. Bian, T. Wang, X. Zhu, H. Liu, Y. Yue, L. Chen, G. Wang, W. Huang, X. Yu, S. Yu, Opto/thermoreactive multimode luminescence in Eu- and Er-activated CaF₂ phosphor for high-security anticounterfeiting, *ACS Appl. Mater. Inter.* 16 (2024) 57346–57354.
- [22] Y. Tian, R. Hua, J. Yu, J. Sun, B. Chen, The effect of excitation power density on frequency upconversion in Yb³⁺/Er³⁺ codoped Gd₃WO₁₂ nanoparticles, *Mater. Chem. Phys.* 133 (2012) 617–620.
- [23] J.A. Rivera-García, J. Mosqueira-Yauri, T.K. Gundu Rao, E.A. Canaza-Mamani, G. Fiorini, J.F. Benavente, C.D. Gonzales-Lorenzo, J.F.D. Chubaci, S. Watanabe, J. S. Ayala-Arenas, N.F. Cano, Synthesis and thermoluminescence of Ce-doped CaF₂ phosphor: Study of defect centers responsible for the TL emission by EPR analysis, *J. Lumin.* 261 (2023) 119906.
- [24] Y.-H. Zhao, M.-Y. Zong, J.-H. Dong, Z. Zhang, J.-J. Liu, J. Liu, L.-B. Su, Mid-infrared lightly Er³⁺-doped CaF₂ laser under acousto-optical modulation, *Chin. Phys. B* 32 (2023) 034203.
- [25] R.-P. Chai, D.-L. Gao, Q. Pang, D.-H. Hao, The dependence of EPR g-factors on the local structure for tetragonal Nd³⁺ and Er³⁺ centers in CaF₂ crystals, *Comput. Theor. Chem.* 1219 (2023) 113967.
- [26] W. Lv, J. Ye, Q. Wang, C. Li, J. Wang, Z. Zhang, N. Niu, Z. Liu, J. Xu, Y. Fu, Tumor-responsive upconversion nanoparticles with tunable degradability and ultrabright emission for optical bioimaging, *ACS Appl. Nano Mater.* 5 (2022) 9367–9378.
- [27] Y. Yang, Z. Zhou, B. Mei, Y. Zhang, X. Liu, Fabrication and upconversion luminescence properties of Er:SrF₂ transparent ceramics compared with Er:CaF₂, *Ceram. Int.* 47 (2021) 17139–17146.
- [28] N. Rakov, F. Matias, G.S. Maciel, Temperature sensing performance of Er³⁺:Yb³⁺ co-doped CaF₂ ceramic powders using near-infrared light, *J. Rare Earth* 43 (2025) 253–261.
- [29] A.A. Ansari, M.A.M. Khan, B.P. Singh, A.K. Parchur, Upconversion nanoparticles: influence of the host lattices on crystallographic and luminescent properties, *J. Mater. Sci. Mater. El* 34 (2023) 1625.
- [30] Z. Liu, M. Jia, G. Yi, B. Mei, Q. Jing, P. Liu, Fabrication and microstructure characterizations of transparent Er:CaF₂ composite ceramic, *J. Am. Ceram. Soc.* 102 (2018) 285–293.
- [31] S. Hou, Y. Zou, X. Liu, X. Yu, B. Liu, X. Sun, Y. Xing, CaF₂ and CaF₂:Ln³⁺(Ln = Er, Nd, Yb) hierarchical nanoflowers: hydrothermal synthesis and luminescent properties, *CrystEngComm* 13 (2011) 835–840.
- [32] S.E. Hatch, W.F. Parsons, R.J. Weagley, Hot-pressed polycrystalline CaF₂:Dy²⁺ LASER, *Appl. Phys. Lett.* 5 (1964) 153–154.
- [33] K. Suzuki, M. Cadatal-Raduban, M. Kase, S. Ono, Band gap engineering of Ca_xSr_{1-x}F₂ and its application as filterless vacuum ultraviolet photodetectors with controllable spectral responses, *Opt. Mater.* 88 (2019) 576–579.
- [34] M. Anandkumar, A. Lathe, A.M. Palve, A.S. Deshpande, Single-phase Gd_{0.2}La_{0.2}Ce_{0.2}Hf_{0.2}Zr_{0.2}O₂ and Gd_{0.2}La_{0.2}Y_{0.2}Hf_{0.2}Zr_{0.2}O₂ nanoparticles as efficient photocatalysts for the reduction of Cr(VI) and degradation of methylene blue dye, *J. Alloy. Compd.* 850 (2021) 156716.
- [35] A.A. Ansari, R. Yadav, S.B. Rai, Physiochemical properties of greatly enhanced photoluminescence of aqueous dispersible upconversion CaF₂:Yb/Er nanoparticles, *Photoch. Photobio. Sci.* 16 (2020) 890–896.